On a fully implicit, monolithic FEM-multigrid solution approach for dynamic porous media problems

Stefan Turek[1], Abdulrahman Obaid[1],* and Bernd Markert[2]

[1]*Institute of Applied Mathematics (LS3), Dortmund University of Technology, Vogelpothsweg 87, 44227 Dortmund, Germany and*
[2]*Institute of General Mechanics (IAM), RWTH Aachen University, 52062 Aachen, Germany*

(Dated: September 9, 2013)

We present a novel fully implicit, monolithic multigrid-based finite element solution scheme to efficiently solve the governing set of differential algebraic equations of incompressible poro-elastodynamics. Thereby, we proceed from a two-dimensional, biphasic, saturated porous medium model with intrinsically coupled and incompressible solid and fluid constituents. Our approach, motivated by well-accepted CFD techniques and originally developed for the efficient simulation of incompressible flow problems, is characterized by the following aspects: (1) a special treatment of the algebraically coupled volume balance equation leading to a reduced form of the boundary conditions; (2) usage of a higher-order accurate mixed LBB-stable finite element pair with piecewise discontinuous pressure for the spatial discretization; (3) application of the fully implicit second-order Crank-Nicolson scheme for the time discretization; (4) use of a special monolithic multigrid solver for the resulting discrete linear equation system. For the purpose of validation and to expose the merits and benefits of our new solution strategy in comparison to other established approaches, canonical one- and two-dimensional wave propagation problems are solved. Finally, a large-scale, dynamic soil-structure interaction problem serves to reveal the efficiency of the special multigrid solver in combination with the chosen finite element discretization.

Keywords: Multi-grid solver, Porous media dynamics (PMD), Coupled problem, Implicit-monolithic solution, Finite Element Method (FEM), Computational fluid dynamics (CFD).

1. INTRODUCTION

The numerical solution of large-scale problems of continuum physics is, thanks to modern hard- and software resources, nothing particular. Even many of the more demanding coupled problems that incorporate additional field quantities and may comprise millions of interconnected evolution equations can be effectively solved on complex three-dimensional geometries by resource to distributed and parallel computing. However, such multi-field problems loose their nature of being solved in a straightforward manner if the underlying set of coupled partial differential equations (PDEs) includes algebraic equations representing some essential side condition or Lagrangian constraint, for instance, forcing incompressibility or continuity. This typically leads to ill-conditioned saddle-point problems, which become even more vulnerable to stability and robustness issues if they are accompanied by a certain roughness of the model parameters associated with a tight coupling of the equations [1]. In this regard, the Finite Element Method (FEM) has been proven to provide a suitable variational approximation framework for the numerical treatment of coupled PDE systems that model some continuum-mechanical initial-boundary-value problems. However, the key ingredients to the fast solution of constrained multi-field problems require both a well-conceived FEM discretization, which meets the anticipated accuracy and stability requirements, and a sophisticated fast solver of multigrid type that can handle systems with large condition numbers, thereby outperforming common single-grid methods. Especially for PDEs with elliptic character, due to the incompressibility, hierarchical multigrid techniques as pure solvers or as preconditioners in Krylov-space solvers have proven their advantageous convergence behavior since they may lead to iteration numbers independent of the problem size. This property allows to design highly efficient solution schemes, particularly for large problem sizes.

This is exactly what is required in the case of porous media dynamics (PMD), where the coupling of the displacement, velocity and pressure fields is inherent in the balance equations and controlled by the hydraulic conductivity. From a computational perspective, the most challenging situation is given if the solid and fluid constituents are materially incompressible, the hydraulic conductivity is very low implying a strong coupling and no restriction to the considered frequency range exists, such that reduced displacement-pressure formulations are not feasible. Then, the pore-fluid pressure as algebraic variable takes over the role of a Lagrange multiplier associated with the continuity-like volume balance yielding a system of differential-algebraic equations (DAEs) of higher differentiation index, readily complicating the numerical solution [2]. This is the point of departure of this paper. Here, it is our objective to exploit the formal similarities of the model equations of computational fluid dynamics (CFD), namely the incompressible Navier-Stokes equations, and PMD, and to adopt the sophisticated, high-performance solution strategies of the former to solve large-scale wave-propagation problems in deformable, fluid-saturated poroe-

*Corresponding author. Email: abdulrahman.obaid@math.tu-dortmund.de, Tel.: +49-231-755-3075, Fax: +49-231-755-5933.

lastic solids. Actually, there is an unabated demand for fast simulation of large-scale PMD problems, where especially the transient response of saturated porous materials in the fields of geomechanics, coastal engineering, seismology and also biomechanics is of considerable practical importance. As examples, consider the hazardous impact of seismically-induced soil liquefaction on structures or the use of ultrasound elastography for the non-invasive characterization of soft biological tissues.

For the theoretical description of different physical phenomena in porous materials, the use of multiphasic continuum mechanics is a standard practice. In this regard, when deformable porous solids are concerned, the Theory of Porous Media (TPM) is proven to provide a consistent and well-elaborated macroscopic modeling framework, see [3–5] for details and references. Another popular macroscopic approach to model porous materials, which is based on a generalization of the theory of elasticity, is Biot's Theory (BT) [6, 7]. In fact, BT, the TPM and derivatives thereof are considered as the bases of many later works in the modeling of dynamic porous media problems, see [8–18] among others. Concerning the applied numerical solution strategies, fully implicit, monolithic solutions using the mixed FEM [19] are well-established and for static porous media problems go back to [20], who have intuitively chosen a LBB-stable quadratic displacement and linear pressure interpolation. Alternative approaches already borrow their ideas from CFD by avoiding the problem with the algebraic pressure variable (cf. [21, 22]). This led to tailored splitting and fractional-step algorithms [2, 23, 24] as well as pressure-stabilization and penalty methods [25, 26] with all known pros and cons. However, as far as the authors are aware, the latest advances in the monolithic solution of generalized incompressible flow problems, that means in conjunction with multiphase flow behaviour and complex rheologies (see [27, 28]), using a special treatment of the algebraic equation in junction with a particular higher-order mixed FE formulation and a fast multigrid solver for the ill-conditioned linear system have not yet been applied to PMD problems.

The paper is structured as follows. Section 2 briefly presents the basics of the TPM approach and provides the governing model equations of poro-elastodynamics. In Section 3, the numerical treatment of the coupled problem is described including the weak formulation, the spatial and temporal discretization as well as the final matrix system. Section 4 is concerned with the numerical validation of the proposed solution strategy by comparing the results of 1D and 2D benchmark simulations with published data. The multigrid solver is then discussed in Section 5, and Section 6 presents a large-scale, 2D, dynamic soil-structure interaction problem simulated with more than 10 million unknowns on the finest mesh level. Finally, Section 7 gives a brief summary and conclusions of the presented research work.

2. THEORETICAL FUNDAMENTALS

In preparation of the numerical treatment, the governing equations of porous media dynamics are briefly recapitulated. This includes the porous media modeling approach, the corresponding kinematics as well as the equilibrium and constitutive relations. For a more detailed discussion, the interested reader is referred to [2, 10, 12] and the citations therein.

2.1. Macroscopic porous media approach

In the framework of the Theory of Porous Media (TPM) [4], we proceed from a continuum-mechanical description of a fluid-filled porous body consisting of a solid matrix saturated by a single pore fluid. Thereby, the binary aggregate is treated as a macroscopic mixture φ with overlaid and interacting but de facto immiscible solid and fluid constituents φ^α ($\alpha = S$: solid; $\alpha = F$: fluid), so that $\varphi = \varphi^S \cup \varphi^F$ at any macroscopic spatial point $\mathbf{x}(t)$ at any time $t \in [t_0, T]$. The local composition of the biphasic continuum is described by volume fractions $n^\alpha(\mathbf{x}, t) := \mathrm{d}v^\alpha / \mathrm{d}v \in (0, 1)$ of φ^α (n^S : solidity; n^F : porosity) defined as the ratios of the partial to the total volume elements of φ. Assuming fully saturated conditions, the saturation constraint obviously yields $\sum_\alpha n^\alpha = n^S + n^F = 1$. Closely related is the introduction of two density functions, namely an effective density $\rho^{\alpha R}(\mathbf{x}, t)$ and a partial density $\rho^\alpha(\mathbf{x}, t)$ relating the local mass of φ^α to the partial or the bulk volume element, respectively. It is easily seen that $\rho^\alpha = n^\alpha \rho^{\alpha R}$ is revealing the general compressibility of porous solids through possible changes of the pore space.

Following the kinematics of mixtures, the superimposed continuum formulation proceeds from unique individual states of motion with each constituent having its own velocity and acceleration field

$$\mathbf{v}_\alpha := \overset{\prime}{\mathbf{x}}_\alpha , \quad (\mathbf{v}_\alpha)'_\alpha = \overset{\prime\prime}{\mathbf{x}}_\alpha \quad \text{with}$$
$$(\bullet)'_\alpha := \frac{\mathrm{d}_\alpha(\bullet)}{\mathrm{d}t} = \frac{\partial(\bullet)}{\partial t} + \operatorname{grad}(\bullet) \cdot \mathbf{v}_\alpha \tag{1}$$

as the material time derivative following the motion of φ^α and $\operatorname{grad}(\bullet) = \partial(\bullet)/\partial\mathbf{x}$. In porous media theories, it is convenient to proceed from a Lagrangian description of the solid matrix via the solid displacement $\mathbf{u}_S$ and velocity $\mathbf{v}_S$ as the kinematical variables. However, the pore-fluid flow is expressed either in a modified Eulerian setting via the seepage velocity vector $\mathbf{w}_{FS}$ describing the fluid motion relative to the deforming skeleton, or by an Eulerian description using the fluid velocity $\mathbf{v}_F$ itself. In particular, we have

$$\mathbf{u}_S = \mathbf{x} - \mathbf{X}_S , \quad \mathbf{v}_S = (\mathbf{u}_S)'_S = \overset{\prime}{\mathbf{x}}_S ,$$
$$\mathbf{v}_F = \overset{\prime}{\mathbf{x}}_F , \quad \mathbf{w}_{FS} = \mathbf{v}_F - \mathbf{v}_S \tag{2}$$

with $\mathbf{X}_S$ representing the reference position vector of the solid phase at time t_0.

2.2. Equilibrium and constitutive relations

The considered biphasic model excludes thermal effects as well as mass exchanges (inert φ^α) and proceeds from intrinsically incompressible constituents ($\rho^{\alpha R} = \text{const.}$). In particular, the arising purely mechanical, binary model with $\alpha = \{S, F\}$ is governed by the following constituent balance equations:

- Partial mass balance $\longrightarrow$ partial volume balance:

$$\begin{aligned} &(\rho^\alpha)'_\alpha + \rho^\alpha \operatorname{div} \mathbf{v}_\alpha = 0 \\ &\quad \longrightarrow \quad (n^\alpha)'_\alpha + n^\alpha \operatorname{div} \mathbf{v}_\alpha = 0 \end{aligned} \tag{3}$$

- Partial momentum balance:

$$\rho^\alpha (\mathbf{v}_\alpha)'_\alpha = \operatorname{div} \mathbf{T}^\alpha + \rho^\alpha \mathbf{b} + \hat{\mathbf{p}}^\alpha \tag{4}$$

Here, $\operatorname{div}(\bullet)$ is the divergence operator related to $\operatorname{grad}(\bullet)$, $\mathbf{T}^\alpha = (\mathbf{T}^\alpha)^T$ is the symmetric partial Cauchy stress assuming non-polar constituents, $\mathbf{b}$ is the mass-specific body force acting on the overall aggregate, and $\hat{\mathbf{p}}^\alpha$ denotes the direct momentum production, which can be interpreted as the volume-specific local interaction force between the percolating pore fluid and the solid skeleton. Due to the overall conservation of momentum, $\hat{\mathbf{p}}^S + \hat{\mathbf{p}}^F = \mathbf{0}$ must hold for any closed multiphasic system. From (3) with $\alpha = S$ and $(n^S \rho^{SR})'_S = (n^S)'_S \rho^{SR}$, one directly obtains the solidity as a secondary variable by integration

$$(n^S)'_S = -n^S \operatorname{div} \mathbf{v}_S \quad \longrightarrow \quad n^S = n^S_{0S} \det \mathbf{F}_S^{-1} \tag{5}$$

with n^S_{0S} being the initial volume fraction of φ^S at time t_0 and $\mathbf{F}_S = \partial \mathbf{x} / \partial \mathbf{X}_S$ as the solid deformation gradient. Proceeding from a small strain approach, n^S can be written in geometrically linear form as

$$n^S \approx n^S_{0S} \left(1 - \operatorname{div} \mathbf{u}_S\right). \tag{6}$$

To continue, according to the principle of effective stresses, see [29] for references, $\mathbf{T}^\alpha$ and $\hat{\mathbf{p}}^F$ can be split into effective field quantities, the so-called extra terms indicated by the subscript $(\bullet)_E$, and parts that are governed by the pore-fluid pressure p

$$\mathbf{T}^\alpha = \mathbf{T}^\alpha_E - n^\alpha p \mathbf{I}, \quad \hat{\mathbf{p}}^F = \hat{\mathbf{p}}^F_E + p \operatorname{grad} n^F \tag{7}$$

with $\mathbf{I}$ being the second-order identity tensor. With regard to a thermodynamically consistent model, admissible constitutive equations for the response functions $\mathbf{T}^\alpha_E$ and $\hat{\mathbf{p}}^F_E$ must be provided. Restricting the presentation to the small strain regime, the solid extra stress is determined by the Hookean elasticity law

$$\begin{aligned} &\mathbf{T}^S_E = 2\mu^S \boldsymbol{\varepsilon}_S + \lambda^S (\boldsymbol{\varepsilon}_S \cdot \mathbf{I}) \mathbf{I} \qquad \text{with} \\ &\boldsymbol{\varepsilon}_S = \tfrac{1}{2} (\operatorname{grad} \mathbf{u}_S + \operatorname{grad}^T \mathbf{u}_S) \end{aligned} \tag{8}$$

as the geometrically linear solid strain tensor and μ^S, λ^S being the macroscopic Lamé constants of the porous solid matrix. Furthermore, under the assumption of isotropic lingering flow conditions at low Reynolds numbers, the percolation process is appropriately described by a linear Darcy-type filter law, which can be traced back to the simple but thermodynamically consistent ansatz

$$\hat{\mathbf{p}}^F_E = -\frac{(n^F)^2 \gamma^{FR}}{k^F} \mathbf{w}_{FS}, \tag{9}$$

where $k^F > 0$ denotes the conventional hydraulic conductivity (Darcy permeability) in m/s and $\gamma^{FR} = \rho^{FR} g$ is the effective fluid weight with $g = |\mathbf{b}|$ denoting the constant scalar gravitational acceleration. Moreover, using (1), the material time derivative with respect to the fluid motion can be written as

$$(\bullet)'_F = (\bullet)'_S + \operatorname{grad}(\bullet) \cdot \mathbf{w}_{FS}. \tag{10}$$

In summary, inserting the aforementioned constitutive and kinematic relations into (4), the governing set of partial differential equations (PDE) reads:

- Balance of momentum of the solid phase

$$\begin{aligned} &\rho^S (\mathbf{v}_S)'_S = \operatorname{div} \mathbf{T}^S_E - n^S \operatorname{grad} p + \rho^S \mathbf{b} \\ &+ \frac{(n^F)^2 \gamma^{FR}}{k^F} (\mathbf{v}_F - \mathbf{v}_S) \end{aligned} \tag{11}$$

- Balance of momentum of the fluid phase

$$\begin{aligned} &\rho^F (\mathbf{v}_F)'_S = \operatorname{div} \mathbf{T}^F_E - n^F \operatorname{grad} p + \rho^F \mathbf{b} \\ &- \frac{(n^F)^2 \gamma^{FR}}{k^F} (\mathbf{v}_F - \mathbf{v}_S) \\ &- \rho^F (\operatorname{grad} \mathbf{v}_F)(\mathbf{v}_F - \mathbf{v}_S) \end{aligned} \tag{12}$$

- Volume balance of the overall aggregate

$$\operatorname{div}(n^F \mathbf{v}_F) + \operatorname{div}(n^S \mathbf{v}_S) = 0 \tag{13}$$

Note that the chosen primary unknowns for this set of PDE are $\mathbf{u}_S$, $\mathbf{v}_F$ and p. Hence, $\mathbf{v}_S(\mathbf{u}_S)$ as well as $\mathbf{T}^S_E(\mathbf{u}_S)$, $\mathbf{T}^F_E(\mathbf{v}_F)$, $n^S(\mathbf{u}_S)$, $n^F(\mathbf{u}_S)$ and $\mathbf{w}_{FS}$ represent the secondary variables of the problem. Additionally, a reduction in the order of the PDE to order-one in time is achieved using

$$(\mathbf{u}_S)'_S = \mathbf{v}_S, \tag{14}$$

which eliminates the second time derivative of the solid displacement from (11), and allows the applicability of a wide range of fundamental time-stepping algorithms.

2.3. Reduction of the complete set of model equations

For the purpose of simplification, several terms in equations (11)-(13) have been neglected, which are marked with blue and red color in the following description:

$$\rho^S (\mathbf{v}_S)'_S = \operatorname{div} \mathbf{T}^S_E - n^S \operatorname{grad} p + \rho^S \mathbf{b} + \frac{(n^F)^2 \gamma^{FR}}{k^F} (\mathbf{v}_F - \mathbf{v}_S) , \tag{15}$$

$$\rho^F (\mathbf{v}_F)'_S + \rho^F (\operatorname{grad} \mathbf{v}_F)(\mathbf{v}_F - \mathbf{v}_S) = \operatorname{div} \mathbf{T}^F_E - n^F \operatorname{grad} p + \rho^F \mathbf{b} - \frac{(n^F)^2 \gamma^{FR}}{k^F} (\mathbf{v}_F - \mathbf{v}_S) , \tag{16}$$

$$\operatorname{grad} n^F \cdot \mathbf{v}_F + \operatorname{grad} n^S \cdot \mathbf{v}_S + n^F \operatorname{div} \mathbf{v}_F + n^S \operatorname{div} \mathbf{v}_S = 0 . \tag{17}$$

Here, n^S and n^F are assumed to be constant, which is acceptable for the small deformation case, such that the blue terms are dropped out. Furthermore, proceeding from a geometrically linear description, the (red) nonlinear convective term can be omitted by scaling arguments if $\operatorname{grad}(\bullet) \cdot \mathbf{w}_{FS} \ll (\bullet)'_S$ yielding $(\bullet)'_F \approx (\bullet)'_S$. To continue with linear PDEs, the pore fluid is assumed to be Newtonian and incompressible leading to the constitutive relation

$$\operatorname{div} \mathbf{T}^F_E = \nu^F \Delta \mathbf{v}_F . \tag{18}$$

In spite of its negligible influence (cf. [30]) in all our performed numerical tests so far, this term containing the (small) fluid viscosity ν^F is nevertheless considered in our subsequent discretization and solution approaches, particularly in view of future large scale simulations which shall be able to involve all physically relevant effects.

3. WEAK FORMULATION AND DISCRETIZATION IN SPACE AND TIME

Our subsequent variational form of the $\mathbf{u}v p$ approach, inspired by weak formulations that are typical in the CFD community for treating the incompressible Navier-Stokes equations, is created by multiplying (15)-(17) with the displacement test function $\delta \mathbf{u}_S$, the velocity test function $\delta \mathbf{v}_F$, the pressure test function δp, integrating over the whole domain Ω and performing partial integrations. Finally, we obtain the following weak form, which is similar to the standard one for porous media (see, for instance, page 1349 of [2]):

$$\begin{aligned} &\int_\Omega \operatorname{grad} \delta \mathbf{u}_S : \mathbf{T}^S_E \, \mathrm{d}v - \int_\Omega n^S \operatorname{div} \delta \mathbf{u}_S \, p \, \mathrm{d}v \\ &- \int_\Omega \frac{(n^F)^2 \gamma^{FR}}{k^F} \delta \mathbf{u}_S \cdot (\mathbf{v}_F - \mathbf{v}_S) \, \mathrm{d}v \\ &+ \int_\Omega \rho^S \delta \mathbf{u}_S \cdot \{ (\mathbf{v}_S)'_S - \mathbf{b} \} \, \mathrm{d}v \\ &= \int_{\Gamma_{\mathbf{t}S}} \delta \mathbf{u}_S \cdot \bar{\mathbf{t}}^S \, \mathrm{d}a \end{aligned} \tag{19}$$

$$\begin{aligned} &\int_\Omega \nu^F \operatorname{grad} \delta \mathbf{v}_F : \operatorname{grad} \mathbf{v}_F \, \mathrm{d}v - \int_\Omega n^F \operatorname{div} \delta \mathbf{v}_F \, p \, \mathrm{d}v \\ &+ \int_\Omega \frac{(n^F)^2 \gamma^{FR}}{k^F} \delta \mathbf{v}_F \cdot (\mathbf{v}_F - \mathbf{v}_S) \, \mathrm{d}v \\ &+ \int_\Omega \rho^F \delta \mathbf{v}_F \cdot \{ (\mathbf{v}_F)'_S - \mathbf{b} \} \, \mathrm{d}v \\ &= \int_{\Gamma_{\mathbf{t}F}} \delta \mathbf{v}_F \cdot \bar{\mathbf{t}}^F \, \mathrm{d}a \end{aligned} \tag{20}$$

$$\int_\Omega n^S \delta p \, \operatorname{div} \mathbf{v}_S \, \mathrm{d}v + \int_\Omega n^F \delta p \, \operatorname{div} \mathbf{v}_F \, \mathrm{d}v = 0 \tag{21}$$

Here, the red-colored terms represent slight differences to [2], namely the additional fluid viscosity term and the natural shape of the weak form of the volume balance. Finally, we multiply (14) with $\delta \mathbf{u}_S$ and integrate over Ω:

$$\int_\Omega \delta \mathbf{u}_S \cdot \{ (\mathbf{u}_S)'_S - \mathbf{v}_S \} \, \mathrm{d}v = 0 . \tag{22}$$

The boundary $\Gamma = \partial \Omega$ is divided into Dirichlet (essential) and Neumann (natural) boundaries, respectively, resulting in $\Gamma = \Gamma_{\mathbf{u}_S} \cup \Gamma_{\mathbf{t}S}$ for the balance of momentum of the solid phase and in $\Gamma = \Gamma_{\mathbf{v}_F} \cup \Gamma_{\mathbf{t}F}$ for the balance of momentum of the fluid phase, wherein the tractions are defined as

$$\bar{\mathbf{t}}^S = (\mathbf{T}^S_E - n^S p \mathbf{I}) \cdot \mathbf{n} , \quad \bar{\mathbf{t}}^F = \nu^F \frac{\partial \mathbf{v}_F}{\partial \mathbf{n}} - n^F p \mathbf{n} . \tag{23}$$

Keep in mind that due to the fact that the pressure (as Lagrange multiplier regarding the incompressibility constraint) provides typically less regularity than displacement and velocity, the pressure derivatives in the weak formulation have been eliminated by partial integration. For the same reason and as usual for the treatment of the incompressible Navier-Stokes equations, no integration by parts has been carried out in (21).

Using such a weak form, which avoids derivatives acting on the pressure functions, one can use standard FEM pairs for velocity/displacement and pressure as typical for

incompressible flow problems, which are based on piecewise discontinuous pressure approximations (as shown in Figure 1), and the boundary conditions are imposed in a slightly modified way in which the fully drained boundaries are represented by the typical CFD 'Do-nothing' (see [31]) boundary condition ($\bar{\mathbf{t}}^F = \mathbf{0}$) while the volume effluxes and values for the pressure as boundary conditions are not needed anymore. Therefore, we can choose the boundary conditions independently. As a candidate for LBB-stable Stokes elements, we apply in the following (2D) simulations the well-known (non-parametric) Q2/P1 element, that means biquadratic velocities and displacements and piecewise linear (discontinuous) pressure approximations (cf. [32]), which belongs currently to the 'best' FEM choices for incompressible flow problems with respect to efficiency, accuracy and robustness.

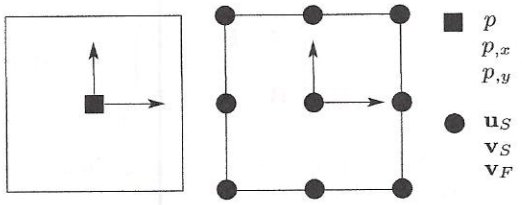

FIG. 1: The discontinuous linear pressure element P1 (left) and the 9-node Lagrange biquadratic element Q2 (right) that are used for the $\mathbf{uv}p(3)$-TR method.

Since we want to show explicit comparisons with a more classical (here: $\mathbf{uv}p$-TB2) approach (see [2]), we additionally introduce the Taylor-Hood-like element in Figure 2, with biquadratic (Q) approximations for some degrees of freedom (DOF) omitting the internal node (serendipity element), and continuous bilinear (L) approximations for other degrees of freedom.

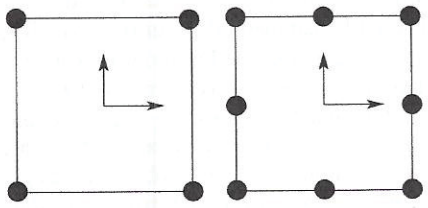

FIG. 2: The standard 4-node bilinear element L (left) and the 8-node serendipity quadrilateral element Q (right) that are used for the $\mathbf{uv}p(2)$-TB2 and $\mathbf{uv}p(2)$-TR method. Three cases are tested: (1) QL: $\mathbf{u}_S$, $\mathbf{v}_S$: biquadratic; $\mathbf{v}_F$, p: bilinear (2) LL: $\mathbf{u}_S$, $\mathbf{v}_S$: bilinear; $\mathbf{v}_F$, p: bilinear (3) QQ: $\mathbf{u}_S$, $\mathbf{v}_S$: biquadratic; $\mathbf{v}_F$, p: biquadratic

Next, based on the discretization with the introduced FEM spaces, equations (19)-(22) can be written in the following matrix-vector notation:

$$\mathbf{M}\dot{\mathbf{y}} + \mathbf{K}\mathbf{y} = \mathbf{f}\,. \tag{24}$$

In more detail with mass and stiffness matrices and right hand side vectors, one obtains with $\mathbf{y}^T = [\,\mathbf{u}_S^T\,\mathbf{v}_S^T\,\mathbf{v}_F^T\,p^T\,]$

$$\begin{pmatrix} \mathbf{M}_{\mathbf{v}_S\mathbf{u}_S} & \mathbf{0} & \mathbf{0} & \mathbf{0} \\ \mathbf{0} & \mathbf{M}_{\mathbf{u}_S\mathbf{v}_S} & \mathbf{0} & \mathbf{0} \\ \mathbf{0} & \mathbf{0} & \mathbf{M}_{\mathbf{v}_F\mathbf{v}_F} & \mathbf{0} \\ \mathbf{0} & \mathbf{0} & \mathbf{0} & 0 \end{pmatrix} \begin{pmatrix} \dot{\mathbf{u}}_S \\ \dot{\mathbf{v}}_S \\ \dot{\mathbf{v}}_F \\ \dot{p} \end{pmatrix} + \tag{25}$$

$$\begin{pmatrix} \mathbf{0} & \mathbf{K}_{\mathbf{v}_S\mathbf{v}_S} & \mathbf{0} & \mathbf{0} \\ \mathbf{K}_{\mathbf{u}_S\mathbf{u}_S} & \mathbf{K}_{\mathbf{u}_S\mathbf{v}_S} & \mathbf{K}_{\mathbf{u}_S\mathbf{v}_F} & \mathbf{K}_{\mathbf{u}_Sp} \\ \mathbf{0} & \mathbf{K}_{\mathbf{v}_F\mathbf{v}_S} & \mathbf{K}_{\mathbf{v}_F\mathbf{v}_F} & \mathbf{K}_{\mathbf{v}_Fp} \\ \mathbf{0} & \mathbf{K}_{p\mathbf{v}_S} & \mathbf{K}_{p\mathbf{v}_F} & 0 \end{pmatrix} \begin{pmatrix} \mathbf{u}_S \\ \mathbf{v}_S \\ \mathbf{v}_F \\ p \end{pmatrix}$$

$$= \begin{pmatrix} \mathbf{0} \\ \mathbf{f}_{\mathbf{u}_S} + \mathbf{b}_S \\ \mathbf{f}_{\mathbf{v}_F} + \mathbf{b}_F \\ 0 \end{pmatrix}$$

with the following matrices and right hand side vectors:

$$\mathbf{K}_{\mathbf{u}_S\mathbf{u}_S} = \int_\Omega \operatorname{grad}\delta\mathbf{u}_S : \mathbf{T}_E^S \, dv$$

$$\mathbf{K}_{\mathbf{u}_S\mathbf{v}_S} = \int_\Omega \frac{(n^F)^2\,\gamma^{FR}}{k^F}\,\delta\mathbf{u}_S \cdot \mathbf{v}_S \, dv$$

$$\mathbf{K}_{\mathbf{u}_S\mathbf{v}_F} = -\int_\Omega \frac{(n^F)^2\,\gamma^{FR}}{k^F}\,\delta\mathbf{u}_S \cdot \mathbf{v}_F \, dv$$

$$\mathbf{K}_{\mathbf{u}_Sp} = -\int_\Omega n^S \operatorname{div}\delta\mathbf{u}_S \, p \, dv$$

$$\mathbf{K}_{\mathbf{v}_S\mathbf{v}_S} = -\int_\Omega \delta\mathbf{u}_S \cdot \mathbf{v}_S \, dv$$

$$\mathbf{K}_{\mathbf{v}_F\mathbf{v}_S} = -\int_\Omega \frac{(n^F)^2\,\gamma^{FR}}{k^F}\,\delta\mathbf{v}_F \cdot \mathbf{v}_S \, dv$$

$$\tilde{\mathbf{K}}_{\mathbf{v}_F\mathbf{v}_F} = \int_\Omega \nu^F \operatorname{grad}\delta\mathbf{v}_F : \operatorname{grad}\mathbf{v}_F \, dv$$

$$\hat{\mathbf{K}}_{\mathbf{v}_F\mathbf{v}_F} = \int_\Omega \frac{(n^F)^2\,\gamma^{FR}}{k^F}\,\delta\mathbf{v}_F \cdot \mathbf{v}_F \, dv$$

$$\mathbf{K}_{\mathbf{v}_F\mathbf{v}_F} = \tilde{\mathbf{K}}_{\mathbf{v}_F\mathbf{v}_F} + \hat{\mathbf{K}}_{\mathbf{v}_F\mathbf{v}_F}$$

$$\mathbf{K}_{\mathbf{v}_Fp} = -\int_\Omega n^F \operatorname{div}\delta\mathbf{v}_F \, p \, dv$$

$$\mathbf{K}_{p\mathbf{v}_S} = \int_\Omega n^S \delta p \operatorname{div}\mathbf{v}_S \, dv$$

$$\mathbf{K}_{p\mathbf{v}_F} = \int_\Omega n^F \delta p \operatorname{div}\mathbf{v}_F \, dv$$

$$
\begin{aligned}
\mathbf{M}_{\mathbf{u}_S\mathbf{v}_S} &= \int_\Omega \left\{n^S\rho^{SR}\right\}\delta\mathbf{u}_S\cdot(\mathbf{v}_S)'_S\,\mathrm{d}v\\
\mathbf{M}_{\mathbf{v}_S\mathbf{u}_S} &= \int_\Omega \delta\mathbf{u}_S\cdot(\mathbf{u}_S)'_S\,\mathrm{d}v\\
\mathbf{M}_{\mathbf{v}_F\mathbf{v}_F} &= \int_\Omega \left\{n^F\rho^{FR}\right\}\delta\mathbf{v}_F\cdot(\mathbf{v}_F)'_S\,\mathrm{d}v\\
\mathbf{f}_{\mathbf{u}_S} &= \int_{\Gamma_{\mathbf{t}^S}} \delta\mathbf{u}_S\cdot\bar{\mathbf{t}}^S\,\mathrm{d}a\\
\mathbf{f}_{\mathbf{v}_F} &= \int_{\Gamma_{\mathbf{t}^F}} \delta\mathbf{v}_F\cdot\bar{\mathbf{t}}^F\,\mathrm{d}a\\
\mathbf{b}_S &= \int_\Omega \left\{n^S\rho^{SR}\right\}\delta\mathbf{u}_S\cdot\mathbf{b}\,\mathrm{d}v\\
\mathbf{b}_F &= \int_\Omega \left\{n^F\rho^{FR}\right\}\delta\mathbf{v}_F\cdot\mathbf{b}\,\mathrm{d}v
\end{aligned}
\tag{26}
$$

In the next step, regarding the time integration, equations (24) or (25) are treated in a monolithic implicit way leading to a fully coupled system. In our approach, we apply the standard one-step θ-scheme to these systems, leading to

$$
\begin{aligned}
\mathbf{M}\frac{\mathbf{y}_{n+1}-\mathbf{y}_n}{\Delta t} + \theta\mathbf{K}\mathbf{y}_{n+1} &= -(1-\theta)\,\mathbf{K}\mathbf{y}_n \\
&\quad + \theta\mathbf{f}_{n+1} + (1-\theta)\mathbf{f}_n\,.
\end{aligned}
\tag{27}
$$

However, as an important remark for the subsequent more detailed description, the red-colored continuity equation due to the incompressibility constraint and the blue-colored pressure p as corresponding Lagrange multiplier are always treated fully implicitly (that means, as usual in CFD simulations, $\theta = 1$), which leads to second-order accuracy (cf. [32]).

$$
\begin{aligned}
&\begin{pmatrix}
\mathbf{M}_{\mathbf{v}_S\mathbf{u}_S} & \theta_1\mathbf{K}_{\mathbf{v}_S\mathbf{v}_S} & 0 & 0\\
\theta_1\mathbf{K}_{\mathbf{u}_S\mathbf{u}_S} & \tilde{\mathbf{A}}_{\mathbf{u}_S\mathbf{v}_S} & \theta_1\mathbf{K}_{\mathbf{u}_S\mathbf{v}_F} & \mathbf{K}_{\mathbf{u}_Sp}\\
0 & \theta_1\mathbf{K}_{\mathbf{v}_F\mathbf{v}_S} & \tilde{\mathbf{A}}_{\mathbf{v}_F\mathbf{v}_F} & \mathbf{K}_{\mathbf{v}_Fp}\\
0 & \mathbf{K}_{\mathrm{pv_S}} & \mathbf{K}_{p\mathbf{v}_F} & 0
\end{pmatrix}
\begin{pmatrix}
\mathbf{u}_S\\ \mathbf{v}_S\\ \mathbf{v}_F\\ \bar{p}
\end{pmatrix}_{n+1}\\
&= \begin{pmatrix}
\mathbf{M}_{\mathbf{v}_S\mathbf{u}_S} & \theta_2\mathbf{K}_{\mathbf{v}_S\mathbf{v}_S} & 0 & 0\\
\theta_2\mathbf{K}_{\mathbf{u}_S\mathbf{u}_S} & \hat{\mathbf{A}}_{\mathbf{u}_S\mathbf{v}_S} & \theta_2\mathbf{K}_{\mathbf{u}_S\mathbf{v}_F} & 0\\
0 & \theta_2\mathbf{K}_{\mathbf{v}_F\mathbf{v}_S} & \hat{\mathbf{A}}_{\mathbf{v}_F\mathbf{v}_F} & 0\\
0 & 0 & 0 & 0
\end{pmatrix}
\begin{pmatrix}
\mathbf{u}_S\\ \mathbf{v}_S\\ \mathbf{v}_F\\ \bar{p}
\end{pmatrix}_n\\
&\quad + \theta_1\mathbf{f}_{n+1} - \theta_2\mathbf{f}_n
\end{aligned}
\tag{28}
$$

with

$$
\begin{aligned}
\theta_1 &= \theta\Delta t\,, \quad \theta_2 = (\theta-1)\Delta t\\
\tilde{\mathbf{A}}_{\mathbf{u}_S\mathbf{v}_S} &= \mathbf{M}_{\mathbf{u}_S\mathbf{v}_S} + \theta_1\mathbf{K}_{\mathbf{u}_S\mathbf{v}_S}\\
\tilde{\mathbf{A}}_{\mathbf{v}_F\mathbf{v}_F} &= \mathbf{M}_{\mathbf{v}_F\mathbf{v}_F} + \theta_1\mathbf{K}_{\mathbf{v}_F\mathbf{v}_F}\\
\hat{\mathbf{A}}_{\mathbf{u}_S\mathbf{v}_S} &= \mathbf{M}_{\mathbf{u}_S\mathbf{v}_S} + \theta_2\mathbf{K}_{\mathbf{u}_S\mathbf{v}_S}\\
\hat{\mathbf{A}}_{\mathbf{v}_F\mathbf{v}_F} &= \mathbf{M}_{\mathbf{v}_F\mathbf{v}_F} + \theta_2\mathbf{K}_{\mathbf{v}_F\mathbf{v}_F}
\end{aligned}
\tag{29}
$$

Note that the time steps (Δt), supposed to be in front of the (blue) pressure matrices, are absorbed into $\bar{p} = \Delta t\, p$, as usually done in CFD, leading to the following saddle-point problem with $\mathbf{U}^T = [\,\mathbf{u}_S^T\,\mathbf{v}_S^T\,\mathbf{v}_F^T\,]$ that we solve for every time step:

$$
\begin{pmatrix}
\tilde{\mathbf{A}} & \mathbf{B}\\
\mathbf{B}^{\mathrm{T}} & 0
\end{pmatrix}
\begin{pmatrix}
\mathbf{U}\\ \bar{p}
\end{pmatrix}_{n+1}
= \mathbf{RHS}
\tag{30}
$$

After solving the above saddle-point system, the pressure is scaled back using the relation $p = \bar{p}/\Delta t$. Setting $\theta = 1/2$, we recover the second-order Crank-Nicolson scheme (in time), which is based on the well-known trapezoidal rule (TR). However, also fully L-stable second-order schemes like BDF(2) or Fractional-Step-Theta-schemes can be used in an analogous way.

4. NUMERICAL VALIDATION

To validate and to evaluate our discussed formulations (which all have been realized in our in-house code FEATFLOW [43]), two numerical examples taken from [2] are introduced and implemented in order to compare with well-established methods. Our **uv**p(3)-TR-Q2/P1 approach stands for the described monolithic solver for the **uv**p formulation based on the weak forms (19)-(22) using the fully implicit Crank-Nicolson ($\theta = 1/2$) time integration scheme as shown in (28) and the mixed finite element pairs Q2/P1 shown in Figure 1. The number 3 in **uv**p(3)-TR-Q2/P1 is used to distinguish our solution algorithms from those in Table I in [2].

4.1. Results I: Saturated poroelastic column under harmonic load

In this example, the response of a homogeneous and isotropic, water-saturated, poroelastic column (height: 10 m, width: 2 m) is analyzed under plane-strain, confined compression conditions. Therefore, the mixture domain is surrounded by impermeable, frictionless but rigid boundaries except for the loaded top side, which is perfectly

drained ($\bar{\mathbf{t}}^F = \mathbf{0}$) [2]. The geometry with boundary conditions and meshes are illustrated in Figure 3, Figure 18 and Table I.

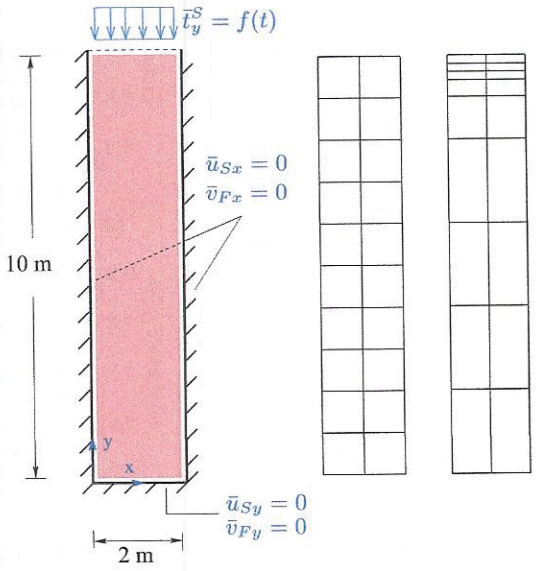

FIG. 3: Geometry, boundary conditions (left) and FE meshes (mesh level 1, isotropic cartesian (center) and rectilinear (right)) of the dynamic confined compression of a saturated poroelastic column. Non prescribed DOFs are automatically taken as natural boundary conditions. $f(t) = 10^3[1 - \cos(20\,\pi\,t)]$ [N/m^2]. For higher mesh levels, see also Figure 18 and Table I.

TABLE I: Total number of elements and unknowns (five primary unknowns u_{Sx}, u_{Sy}, v_{Fx}, v_{Fy} and p plus two secondary unknowns v_{Sx} and v_{Sy}) for the **uv**p(3)-TR-Q2/P1 approach. This table is related to Figure 3 and Figure 18.

Cartesian			Rectilinear		
#Elem./m	#Elem.	#Unknowns	Level	#Elem.	#Unknowns
1	20	690	1	18	625
5	500	14226	2	72	2214
10	2000	55446	3	288	8310
15	4500	123666	4	1152	32166
20	8000	218886	5	4608	126534
25	12500	341106	-	-	-
30	18000	490326	-	-	-
40	32000	869766	-	-	-
50	50000	1357206	-	-	-

The constitutive material parameters are adopted from related literature [33] and listed in Table II. The aim of this simple benchmark problem is to mainly compare our monolithic **uv**p(3)-TR-Q2/P1 approach with the reference solutions for the solid displacement and the pore-fluid pressure obtained by analytically solving the following slightly different 1-dimensional PDEs:

- Balance of momentum of the solid phase:

$$\rho^S u_{S,tt} = \underbrace{(\lambda^S + 2\mu^S) u_{S,yy}}_{\operatorname{div} \mathbf{T}_E^S} - n^S p_{,y} + \frac{(n^F)^2 \gamma^{FR}}{k^F} (u_{F,t} - u_{S,t})$$

- Balance of momentum of the fluid phase:

$$\rho^F u_{F,tt} = -n^F p_{,y} - \frac{(n^F)^2 \gamma^{FR}}{k^F} (u_{F,t} - u_{S,t})$$

- Volume balance of the overall aggregate:

$$n^S u_{S,ty} + n^F u_{F,ty} = 0$$

For further details, see [33].

It also serves to compare the accuracy of our **uv**p(3)-TR-Q2/P1 approach with the classical ones. Here, two scenarios are tested: (1) a high permeability case with $k^F = 10^{-2}$ m/s and (2) a moderately low permeability case with $k^F = 10^{-5}$ m/s, which is the lowest permeability for which the analytical reference solution could be achieved using Maple [2].

TABLE II: Physical properties of the porous medium used for all simulations.

Parameter	Symbol	Value	SI Unit
first Lamé constant of solid	μ^S	5.583×10^6	N/m^2
second Lamé constant of solid	λ^S	8.375×10^6	N/m^2
Effective density of dense solid	ρ^{SR}	2000	kg/m^3
Effective density of pore fluid	ρ^{FR}	1000	kg/m^3
Initial volume fraction of solid	$n^S = n_{0S}^S$	0.67	–
Darcy permeability	k^F	$10^{-2}, 10^{-5}$	m/s
Fluid viscosity (Figure 3 & 11)	ν^F	10^{-3}	Pas
Fluid viscosity (Figure 19)	ν^F	10^{-14}	Pas

Since the optimal time step (that means the maximum time step that leads to a time step independent solution on a given spatial mesh) in our method seems to be mesh independent, our computations are performed on anisotropic meshes that get finer when approaching the top (perfect drainage) boundary since at the top we have $\bar{\mathbf{t}}^F = \mathbf{0}$, which must be compensated by an immediate pressure increase in a small layer below the boundary as stated in [2]. From Figure 4, we note that for each refinement level the optimal time step remains the same (nearly 5×10^{-3} s), which indicates that the optimal time step in our **uv**p(3)-TR-Q2/P1 method is indeed mesh size independent.

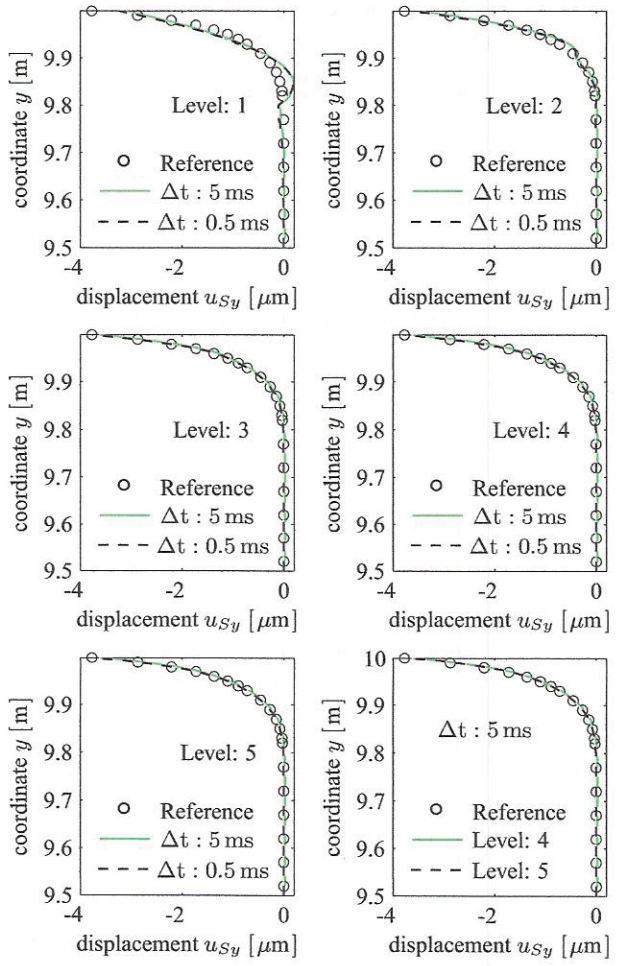

FIG. 4: Solid displacement distribution in the first half meter under the loaded top of the column at time $= 0.15$ s using **uv**p(3)-TR-Q2/P1 for $k^F = 10^{-5}$ m/s and the rectilinear mesh (cf. Figure 3 right). The reference solution is taken from [2].

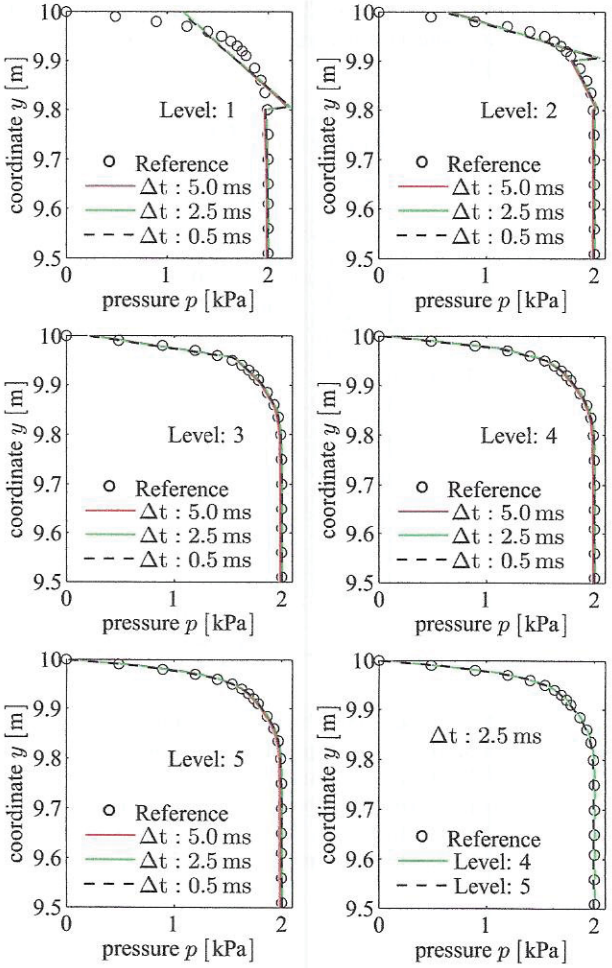

FIG. 5: Pressure distribution in the first half meter under the loaded top of the column at time $= 0.15$ s using **uv**p(3)-TR-Q2/P1 for $k^F = 10^{-5}$m/s and the rectilinear mesh (cf. Figure 3 right). The reference solution is taken from [2].

We notice that the displacement obtains full convergence at a mesh level and time step size where the pressure is still not fully converged (see Figures 4 and 5). This indicates that a small error in the pressure does not significantly influence the full convergence in the displacement. Moreover, from Figures 6 and 7 one can notice that for smaller k^F, i. e. for a stronger coupling, more elements are required to reach full convergence to capture the large gradient in the pressure. However, in both cases the optimal time step does not change. This indicates that the stability of the proposed method is also not influenced by the value of the permeability parameter k^F.

For comparing the accuracy of the **uv**p(3)-TR-Q2/P1 method with the well-established classical methods, we adopt the isotropic Cartesian mesh of Figure 3. Although this kind of mesh requires a larger number of elements, it was opted because the results of the classical methods reported in [2] are based on this discretization. From Figure 8, we notice that for this problem the proposed **uv**p(3)-TR-Q2/P1 method provides the most accurate solutions at all selected heights except at the top permeable loaded boundary ($\bar{\mathbf{t}}^F = \mathbf{0}$ and $\bar{\mathbf{t}}^S = f(t)\,\mathbf{n}$), where nevertheless the solution is sufficiently accurate. Therefore, we closely look at this top loaded permeable boundary part and beginning with the high permeability case ($k^F = 10^{-2}$ m/s), we notice that our formulation yields a convergent approximation of the solid displacement field following the reference solution u_{ref} of a point at the top of the column (Figure 9, top).

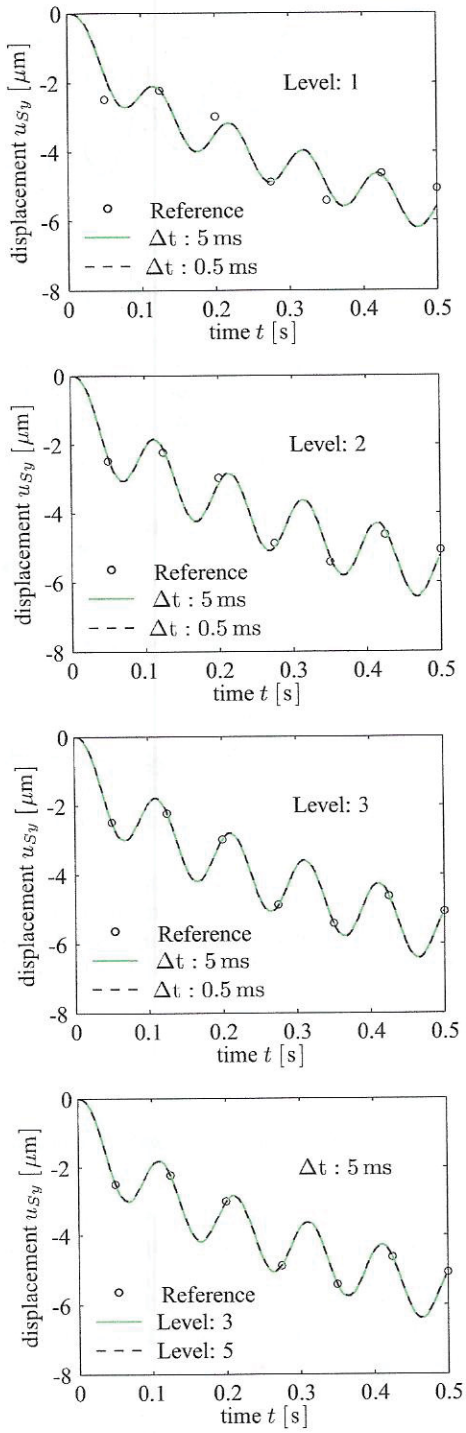

FIG. 6: y-displacement at point (1,10) vs. time using $\mathbf{uv}p(3)$-TR-Q2/P1 for $k^F = 10^{-5}$m/s and rectilinear mesh (cf. Figure 3 right). The reference solution is taken from [2].

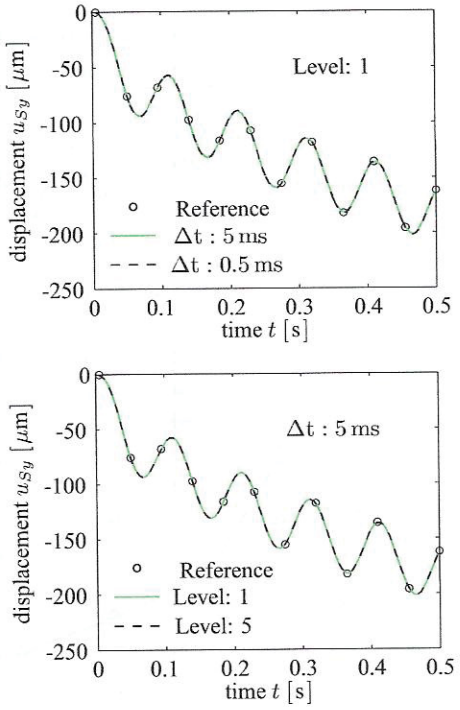

FIG. 7: y-displacement at point (1,10) vs. time using $\mathbf{uv}p(3)$-TR-Q2/P1 for $k^F = 10^{-2}$m/s and rectilinear mesh (cf. Figure 3 right). The reference solution is taken from [2].

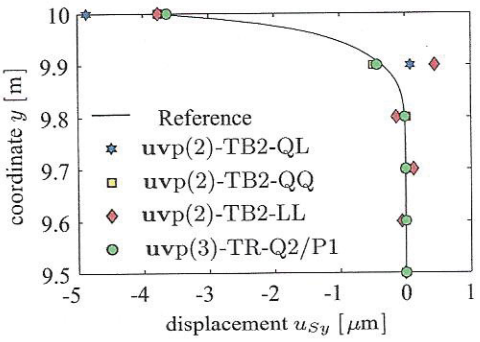

Height	LL	QL	QQ	Q2/P1
9.7	0.12	0.019	0.0055	0.0003
9.8	0.13	0.0062	0.0193	0.0010
9.9	0.8	0.43	0.13	0.077
10	0.00	1.1	0.00	0.13

FIG. 8: Solid displacement (top) and absolute errors in μm (bottom) for the first half meter below the top surface for the isotropic Cartesian mesh (10 elem/m) (cf. Figure 3, center) for $k^F = 10^{-5}$m/s at $t = 0.15$ s. All the data except Q2/P1 are taken from [2].

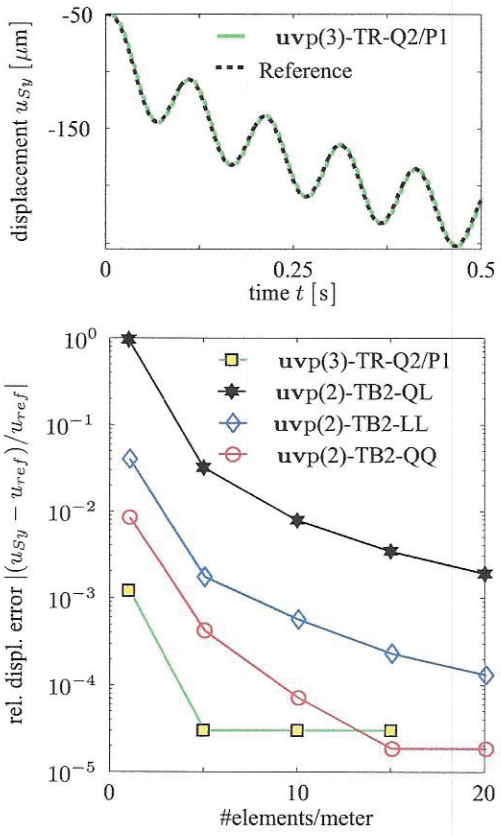

FIG. 9: Top displacement history (top) for $k^F = 10^{-2}$m/s, $t = [0, 0.5]$ s and Cartesian mesh (1 element/meter) using **uvp**(3)-TR-Q2/P1. Relative error (logarithmic scale) over mesh size (bottom) at $t = 0.15$ s. All the data except Q2/P1 are taken from [2].

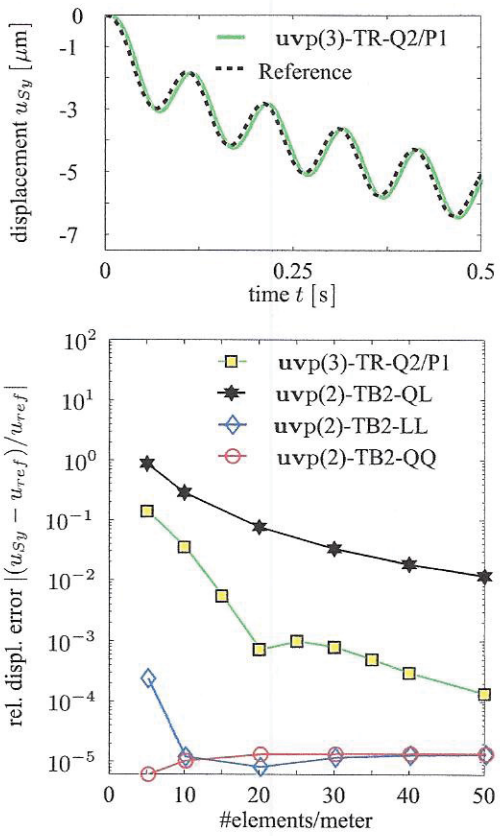

FIG. 10: Top displacement history (top) for $k^F = 10^{-5}$m/s, $t = [0, 0.5]$ s and Cartesian mesh (10 elements/meter) using **uvp**(3)-TR-Q2/P1. Relative error (logarithmic scale) over mesh size (bottom) at $t = 0.15$ s. All the data except Q2/P1 are taken from [2].

Furthermore, regarding the relative displacement error $ERR = |(u_{Sy} - u_{ref})/u_{ref}|$ in Figure 9 (bottom), one observes that the Q2/P1 approach converges faster than the other element pairs (LL, QL and QQ) while QL has the slowest convergence and shows the highest deficiency as expected for large values of k^F [2].

In contrast to the QL approach, we observe a sufficiently accurate displacement solution at the permeable loaded boundary in case of the low permeability (here $k^F = 10^{-5}$m/s) as depicted in Figure 10. The significance of the Q2/P1 approach arises when switching to extremely low permeability values in which both LL and QQ approaches may fail [2] while QL can merely provide insufficient solutions as shown in the following subsection.

4.2. Two-dimensional wave propagation

In this second example, we study the 2D dynamical wave propagation in a rectangular symmetric domain under plane-strain conditions (Figure 11) as presented in [12]. The material parameters are the same as before (Table II) and the 'earthquake event' is represented by the applied distributed impulse force

$$f(t) = 10^5 \sin(25\,\pi\,t)\,[1 - H(t - \tau)]\ [\mathrm{N/m^2}] \qquad (31)$$

with $H(t - \tau)$ being the Heaviside step function and $\tau = 0.04$ s. The water saturated mixture domain is surrounded by impermeable, frictionless ($\bar{t}^F_x = 0$ for the bottom and $\bar{t}^F_y = 0$ for the left and right sides) but rigid boundaries except for the loaded top side, which is perfectly drained ($\bar{\mathbf{t}}^F = \mathbf{0}$).

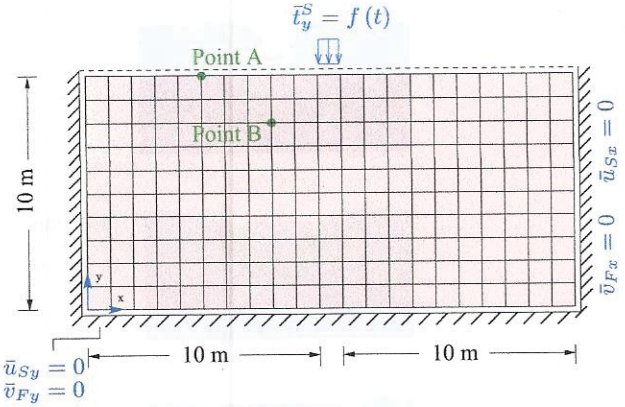

Mesh Level	#Elements (width-height)	#DOFs (Q2/P1)	#DOFs (QL)
1	21-10	6048	3498
2	42-20	23430	13289
3	84-40	92214	51771
4	168-80	365862	102611

FIG. 11: Geometry, boundary conditions and mesh level 1 of the symmetric 2D wave propagation problem (top). Total number of elements and unknowns for the **uv***p*(3)-TR-Q2/P1 approach (bottom). The symmetry of the problem can be exploited to reduce the problem size. However, the computation was performed on the full problem only for our Q2/P1 approach.

The objective of this benchmark problem is to compare quantitatively the accuracy of our proposed monolithic **uv***p*(3)-TR-Q2/P1 approach with **uv***p*(2)-TB2-QL of [2], which is known as well-accepted combination for solving such coupled problems. Here, we study the displacement solution at point A and the pressure history at point B in the high permeability case $k^F = 10^{-2}$ m/s and the extremely low permeability case with $k^F = 10^{-10}$ m/s. In addition, since no analytical solution is available, we validate our results by comparing with [2]. For the high permeability case, we can see from Figure 12 that the optimal time step is approx. 10^{-3} s and the optimum mesh level is already level 2. The direct comparison of the appropriate parameters (mesh level and time step) illustrates the perfect matching as depicted in Figure 13. Note that **uv***p*(2)-TB2-QL obtains the full convergence at level 3 as indicated in Figure 11 of [2] while our **uv***p*(3)-TR-Q2/P1 converges already at mesh level 2 as shown in Figure 12, both leading to similar problem sizes. The subsequent contour plots (Figure 14) generated by our approach in FEATFLOW are very similar to those in [2].

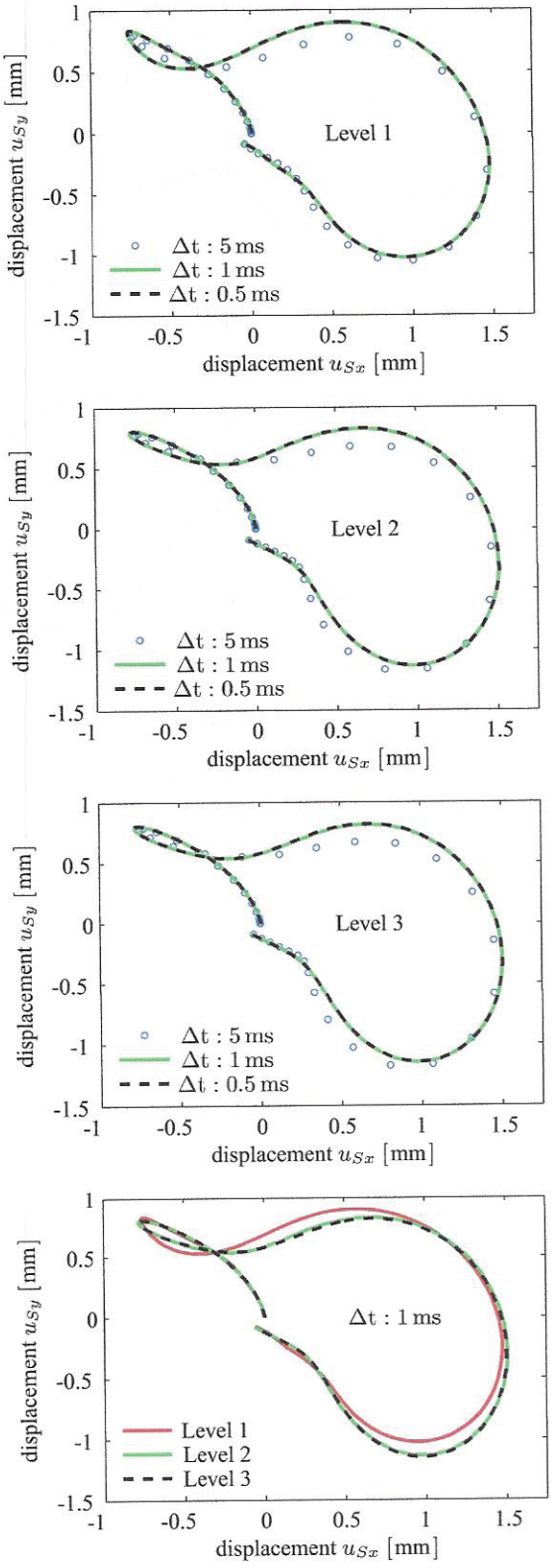

FIG. 12: Ground rolling during the 'earthquake event' at point A using **uv***p*(3)-TR-Q2/P1 with $k^F = 10^{-2}$m/s and $t \in [0\ 0.2]$ s.

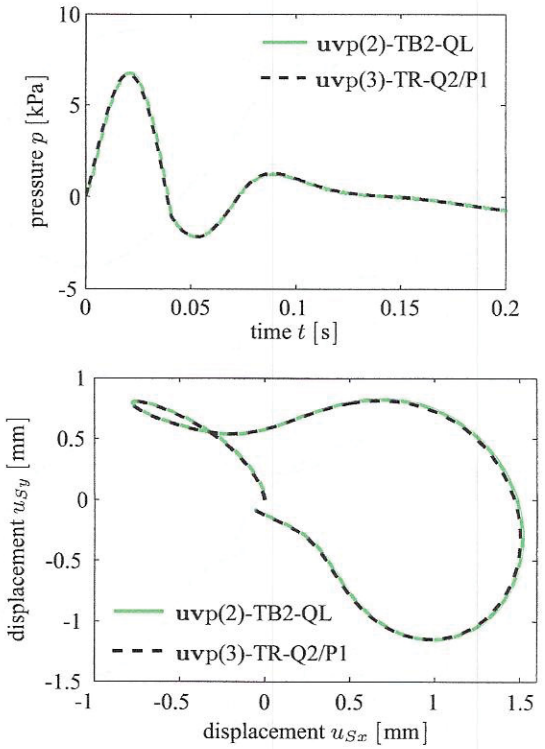

FIG. 13: Pressure history at point B and displacement history at point A using **uvp**(3)-TR-Q2/P1 for $k^F = 10^{-2}$ m/s, $\Delta t = 10^{-3}$ s and mesh level 2. The QL results are taken from [2]

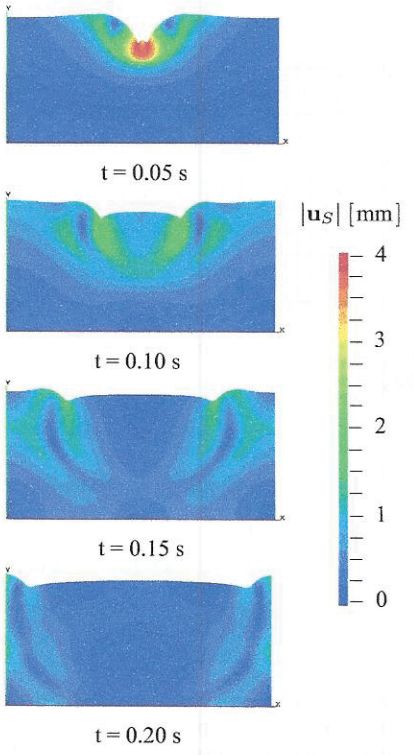

FIG. 14: Time sequence of displacement contour plots with $|\mathbf{u}_S| = \sqrt{u_{Sx}^2 + u_{Sy}^2}$ on the deformed geometry (scaling factor 500) for uvp(3)-TR-Q2/P1, mesh level 4, and $\Delta t = 5 \times 10^{-4}$ s.

Next, we switch to the extremely low permeability of $k^F = 10^{-10}$ m/s, which further demonstrates the merits of the considered Q2/P1 approach. We first conclude the optimal time step ($\Delta t \approx 10^{-3}$ s) and the optimal mesh size (level 2) from Figure 15. For this case both **uvp**(2)-TB2-QQ and **uvp**(2)-TB2-LL do not converge and the monolithic solution requires LBB-stable mixed FE formulations such as QL [2] and Q2/P1 element pairs.

Based on the results shown in Figures 8 and 9, the direct comparison between the QL solutions (on higher mesh levels) and the fully converged Q2/P1 solutions (on mesh level 2) (see Figure 16) reveals the less accurate displacement solution of the QL approach. In contrast to the TR-QL approach, our TR-Q2/P1 approach does not produce large pressure oscillations as seen in Figure 17. Such large oscillations are extremely reduced even for the trapezoidal rule (TR) by using a LBB stable element with equal-order approximations of $\mathbf{u}_S$, $\mathbf{v}_S$ and $\mathbf{v}_F$ such as the Q2/P1 element.

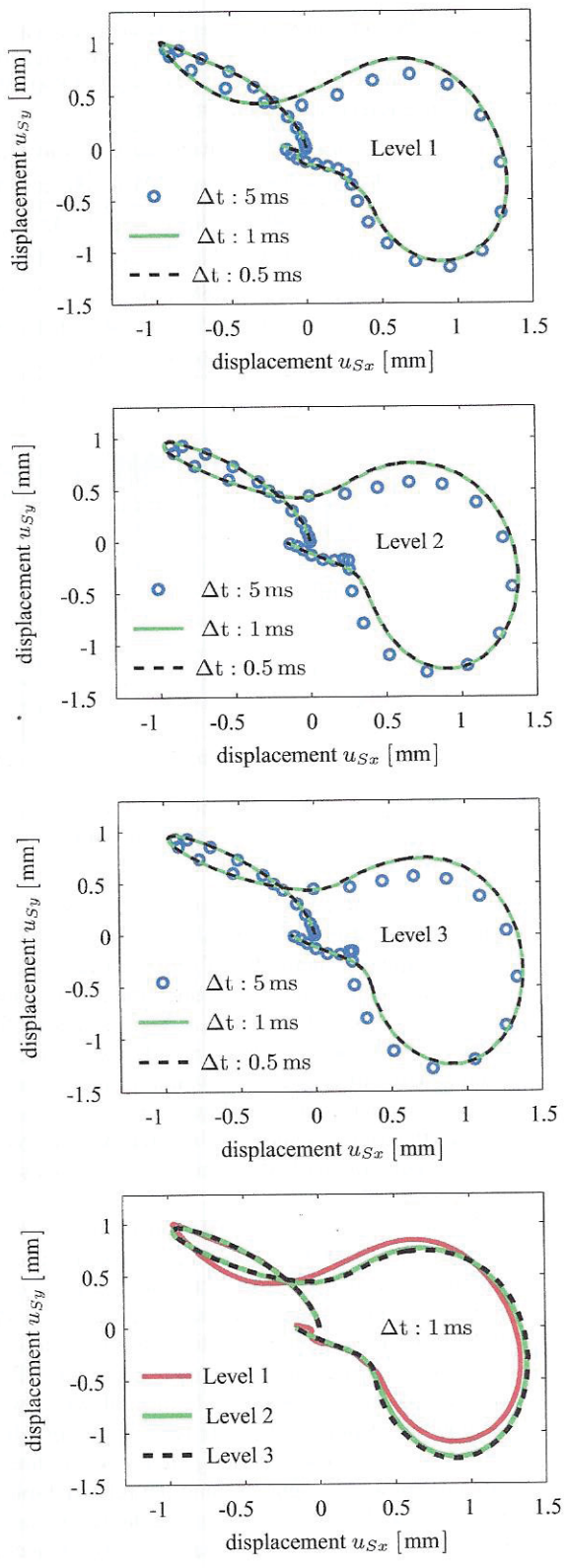

FIG. 15: Ground rolling during the 'earthquake event' at point A using $\mathbf{uv}p(3)$-TR-Q2/P1 with $k^F = 10^{-10}$m/s and $t \in [0\ 0.2]$ s.

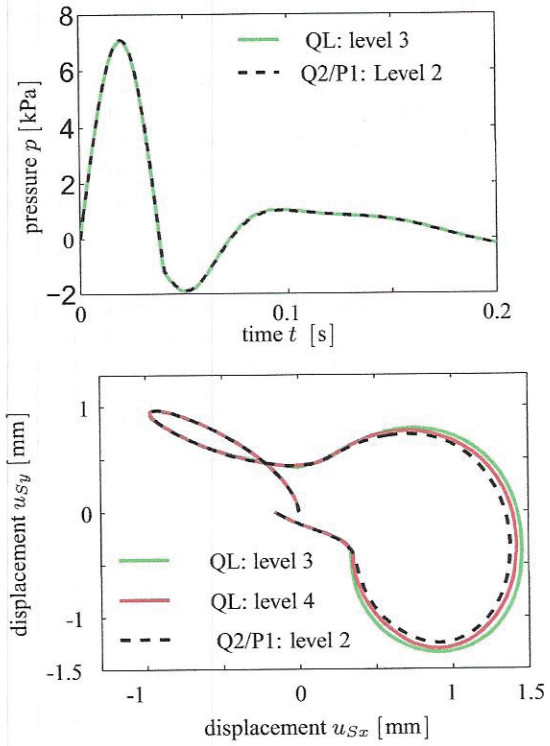

FIG. 16: Pressure history at point B and displacement history at point A using $\mathbf{uv}p(3)$-TR-Q2/P1 and $\mathbf{uv}p(2)$-TB2-QL for $k^F = 10^{-10}$ m/s, $\Delta t = 10^{-3}$ s, $t \in [0\ 0.2]$ s. The results of the QL approach are taken from [2].

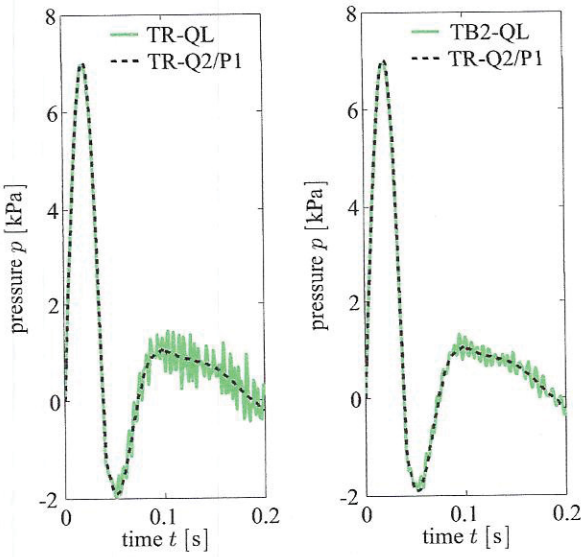

FIG. 17: Pressure history at point B for $k^F = 10^{-10}$ m/s, $\Delta t = 10^{-3}$ s and mesh level 2 for $\mathbf{uv}p(2)$-TB2-QL, $\mathbf{uv}p(2)$-TR-QL and$\mathbf{uv}p(3)$-TR-Q2/P1. The results of the QL approaches are taken from [2].

5. FAST MULTIGRID SOLVERS

During each time step, most of the elapsed CPU time is consumed by solving the corresponding linear systems in (30). Typically, by accuracy reasons which requires small mesh widths, the arising block systems are too large to be handled by direct solvers, such that iterative schemes have to be preferred.

TABLE III: Averaged number of iterations (the first 2 tables) and Averaged CPU time in seconds (the second 2 tables) per time step for the first 10 time steps for preconditioned (by Vanka scheme, see later) BICGSTAB in combination with $\mathbf{uv}p(3)$-TR-Q2/P1 scheme for $k^F = 10^{-2}$ m/s (the first and third table) and $k^F = 10^{-5}$ m/s (the second and fourth table), Residual $< 10^{-8}$, Δt in ms. See Figure 18 for the meshes and Figure 3 for the configuration.

Level	Cartesian		Rectilinear		Unstructured	
	$\Delta t = 5$	$\Delta t = 0.5$	$\Delta t = 5$	$\Delta t = 0.5$	$\Delta t = 5$	$\Delta t = 0.5$
3	31	37	40	41	44	35
4	58	58	79	54	82	47
5	109	54	159	84	162	60

Level	Cartesian		Rectilinear		Unstructured	
	$\Delta t = 5$	$\Delta t = 0.5$	$\Delta t = 5$	$\Delta t = 0.5$	$\Delta t = 5$	$\Delta t = 0.5$
3	31	19	44	19	38	20
4	65	21	130	29	100	32
5	193	32	530	52	368	53

Level	Cartesian		Rectilinear		Unstructured	
	$\Delta t = 5$	$\Delta t = 0.5$	$\Delta t = 5$	$\Delta t = 0.5$	$\Delta t = 5$	$\Delta t = 0.5$
3	1.69	2.01	1.95	2.02	3.84	3.04
4	12.65	12.67	15.37	10.90	28.05	17.03
5	95.75	50.48	125.87	69.82	230.00	90.40

Level	Cartesian		Rectilinear		Unstructured	
	$\Delta t = 5$	$\Delta t = 0.5$	$\Delta t = 5$	$\Delta t = 0.5$	$\Delta t = 5$	$\Delta t = 0.5$
3	1.7	1.02	2.20	0.96	3.30	1.80
4	14.16	4.76	25.40	5.70	34.90	11.80
5	169.90	28.45	418.3	42.00	515.00	76.60

However, due to the nature of the involved partial differential equations, particularly w.r.t. the incompressibility, the condition numbers of the arising matrices typically scale with the problem size and are quite large, such that standard single-grid schemes, for instance Krylov-space methods like BICGSTAB or GMRES (cf. [34, 35]), are too slow, at least for larger problem sizes, and also in the case of larger time step sizes and for spatial meshes with non-equidistant mesh spacing (see Tables III).

TABLE IV: Total number of elements and unknowns (the five primary unknowns: u_{Sx}, u_{Sy}, v_{Fx}, v_{Fy} and p plus the two secondary unknowns: v_{Sx} and v_{Sy}) for $\mathbf{uv}p(3)$-TR-Q2/P1 approach. This table is related to Figure 18.

Level	Cartesian		Rectilinear		Unstructured	
	#Elem.	#DOFs	#Elem.	#DOFs	#Elem.	#DOFs
1	20	690	18	624	32	1038
2	80	2454	72	2214	128	3798
3	320	9222	288	8310	512	14502
4	1280	35718	1152	32166	2048	56646
5	5120	140550	4608	126534	8192	223878

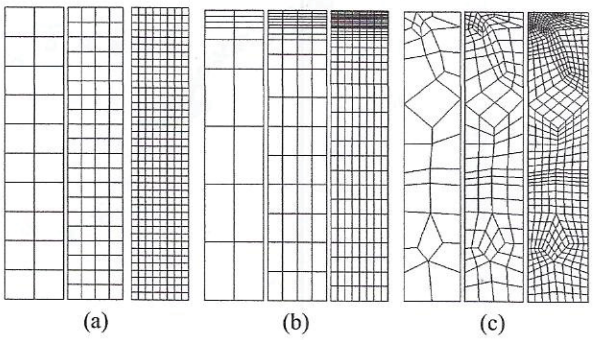

FIG. 18: Mesh level 1, level 2 and level 3 for three kinds of grids: (a) Cartesian, (b) rectilinear and (c) unstructured.

Therefore, an excellent alternative is to solve (30) via geometrical multigrid (MG) solvers (see [28] and [36–38]), which require a hierarchy of refined mesh levels and corresponding intergrid transfer operators, which are selected w.r.t. the chosen FEM spaces. What is special for the described saddle-point problem in (30) is the choice of the so-called 'smoothing operator', which in our case can be traced back to the early work by Vanka [39]. The corresponding (basic) iterative schemes can be interpreted as block Gauß-Seidel methods applied to mixed formulations of saddle-point problems.

These techniques are very prominent in the CFD community to solve incompressible and weakly compressible flow problems, which are based on the (generalized) Navier-Stokes equations. They have been adapted to a wide class of fluidic problems including multiphase flow, fluid-structure interaction, particulate flow, multi-component fluids, flow with chemical reactions, etc. In the following, we perform multigrid iterations of F-cycle type, applying a fixed number of pre- and postsmoothing steps for the three types of grids as shown in Figure 18 and the related Table IV. Typically, we will show results for a sequence of consecutively refined meshes, which are constructed by connecting opposite midpoints of the corresponding coarser meshes, starting from a basic mesh on mesh level 1. The results in the subsequent Table V demonstrate the very efficient con-

vergence behavior for several parameter configurations and they illustrate the typical convergence behavior of multigrid solvers, namely to be more or less independent of the mesh size and the value of k^F. Such independency becomes even more prominent in large-scale problems (see Table VII).

TABLE V: Averaged number of iterations (The first 2 tables) and averaged CPU time in seconds (the second 2 tables) per time step for for the first 10 time steps for MG (F-4-4) for $\mathbf{uv}p$(3)-TR-Q2/P1 for $k^F = 10^{-2}$ m/s (the first and third table) and $k^F = 10^{-5}$ m/s (the second and fourth table), Residual $< 10^{-8}$ and Δt in ms.

Level	Cartesian		Rectilinear		Unstructured	
	$\Delta t = 5$	$\Delta t = 0.5$	$\Delta t = 5$	$\Delta t = 0.5$	$\Delta t = 5$	$\Delta t = 0.5$
3	5	3	12	4	8	4
4	5	3	15	4	13	4
5	5	3	15	4	16	4

Level	Cartesian		Rectilinear		Unstructured	
	$\Delta t = 5$	$\Delta t = 0.5$	$\Delta t = 5$	$\Delta t = 0.5$	$\Delta t = 5$	$\Delta t = 0.5$
3	5	3	13	3	8	3
4	5	3	16	3	13	3
5	5	3	16	4	16	4

Level	Cartesian		Rectilinear		Unstructured	
	$\Delta t = 5$	$\Delta t = 0.5$	$\Delta t = 5$	$\Delta t = 0.5$	$\Delta t = 5$	$\Delta t = 0.5$
3	1.0	0.7	2.2	1.0	2.6	1.2
4	4.4	2.7	11.7	3.8	17.5	5.6
5	20.4	11.5	47.5	16.2	94.3	31.4

Level	Cartesian		Rectilinear		Unstructured	
	$\Delta t = 5$	$\Delta t = 0.5$	$\Delta t = 5$	$\Delta t = 0.5$	$\Delta t = 5$	$\Delta t = 0.5$
3	1.0	0.67	2.4	0.73	2.8	1.1
4	4.5	2.7	12.7	2.6	18.0	4.2
5	19.8	10.7	49.6	13.8	94.3	29.1

6. LARGE-SCALE PROBLEMS

The objective of this section is (1) to test the multigrid solver on a large system with millions of DOFs and (2) to show that the proposed $\mathbf{uv}p$(3)-TR-Q2/P1 method in combination with locally adapted unstructured meshes and mutigrid solution can be an excellent alternative to infinite element extensions in unbounded domain applications.

The advantages of the described multigrid methods become more prominent for porous media applications when working on large-scale problems such as studying the dynamic wave propagation in infinite saturated half spaces. As an example, we adopt the problem of wave propagation in an elastic structure-soil system presented in Section 4.2 of [18]. The problem is illustrated in Figure 19. Such soil-structure interaction problems have been intensively studied in the literature, cf. [40–42].

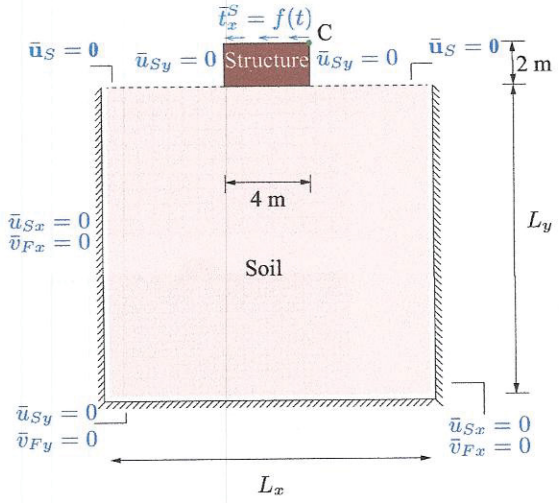

FIG. 19: Geometry of the 2D structure-soil problem with prescribed boundary conditions. The domain is composed of a structure, represented by an elastic block (size: 4×2 m^2), founded on an infinite domain of elastic soil, replaced by a truncated domain (size: $L_x \times L_y$ m^2) with rigid boundaries.

In the current problem, the structure is represented by a block, which is considered to be in a welded contact with the supporting soil. The applied shear impulse force is given by

$$f(t) = 10^4 \left[1 - \cos(20\,\pi\, t)\right] \left[1 - H(t - \tau)\right] \ [\mathrm{N/m^2}] \quad (32)$$

with $H(t-\tau)$ being the Heaviside step function and $\tau = 0.1$ s. The material parameters of the block and the soil are the same (cf. Table II) with $k^F = 10^{-2}$ m/s and both are discretized with the same type of finite elements. This implies a weak damping of the vibrations in the loaded structure resulting in a successive wave transition into the soil [18]. The unbounded soil domain beneath the block is replaced by a finite domain with artificial, impermeable, frictionless but rigid boundaries except for the top side, which is fully drained ($\bar{\mathbf{t}}^F = \mathbf{0}$). Since the acoustic waves in the case of an unbounded domain propagate towards infinity, the vibration of, for example, point C is supposed to progress without being later disturbed by the arrival of the reflected waves resulting from the artificially fixed boundaries. To resolve this issue, the arrival of these 'undesired' waves is delayed by choosing the dimensions ($L_x \times L_y$) of the represented finite domain large enough, so that for a desired period of time, point C can vibrate unimpeded before the unwanted waves travel back and corrupt the solution. This is not an economic way, but it serves the purpose to reveal the capabilities of our solution approach in case of large-scale problems. A more convenient treatment of infinite domain boundaries, for instance, by use of infinite elements

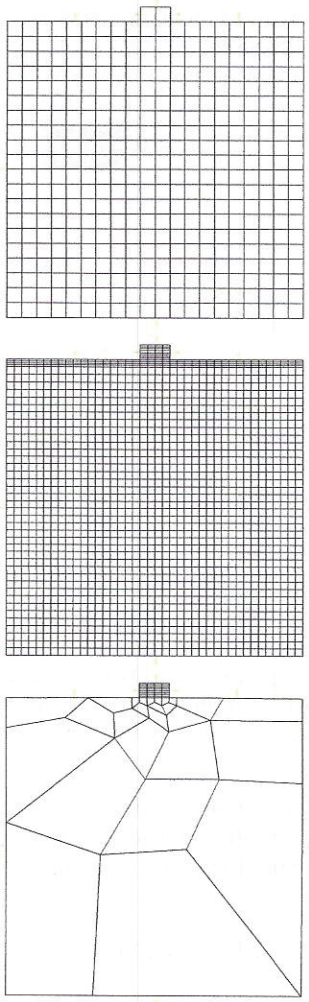

FIG. 20: Level 1 of the Cartesian (top), rectilinear (middle) and unstructured grid (bottom) for the problem in Figure 19. For higher mesh levels, see Tables VI and VII.

in the static form in combination with the viscous damping boundary method is described in [18]. Taking the area (84×81 m^2) as reference, we notice from Figure 21 that the correct description of the horizontal displacement of point C with time is attained by adopting a finite domain of area 20×20 m^2 and 40×40 m^2 for the time intervals $t \in [0\ 0.7]$ s and $t \in [0\ 1.4]$ s, respectively. Following [18], the finite domain size is set to 40×40 m^2 and the time period is set to $t \in [0\ 1.0]$ s. Using such an equidistant (Cartesian) mesh, as done in [18], requires an unnecessarily large number of finite elements, leading to correspondingly large computational costs. The results for different mesh levels are illustrated in Figure 22.

As a remark, with our $\mathbf{uv}p(3)$-TR-Q2/P1 approach using the described multigrid solver, the results for level 3 are available in few hours using a standard PC as shown in Table VI.

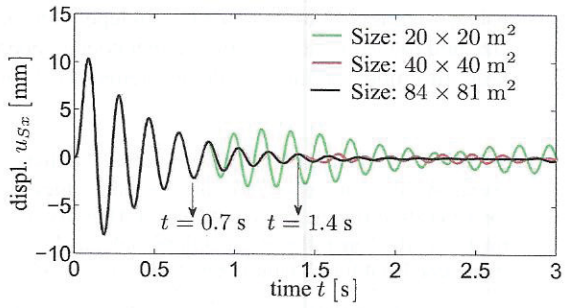

FIG. 21: Time history of the horizontal displacement at point C using $\mathbf{uv}p(3)$-TR-Q2/P1 scheme for level 1 and the rectilinear mesh of Figure 20.

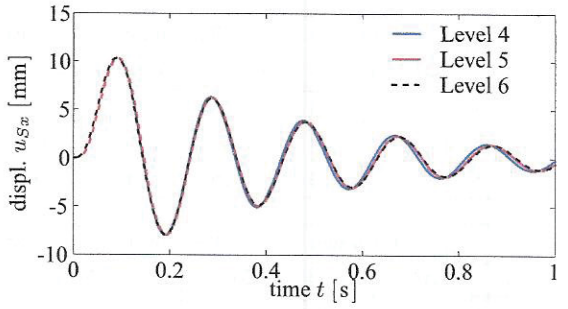

FIG. 22: Time history of the horizontal displacement at point C using $\mathbf{uv}p(3)$-TR-Q2/P1 for $k^F = 10^{-2}$ m/s and the Cartesian grid with optimal time step $\Delta t = 2$ ms. The corresponding number of elements and number of DOFs are given in Table VI.

TABLE VI: Averaged number of iterations (#Iter.) and elapsed CPU time (CPU) in seconds per time step for the described multigrid solver for $\mathbf{uv}p(3)$-TR-Q2/P1 for $t \in [0\ 1.0]$ s and $\Delta t = 2$ ms for the Cartesian grid case and k^F in m/s.

Level	#Elem.	#DOFs	$k^F = 10^{-2}$		$k^F = 10^{-5}$		$k^F = 10^{-10}$	
			#Iter.	CPU	#Iter.	CPU	#Iter.	CPU
2	1608	44406	2	2.5	2	2	2	2
3	6432	175638	3	19	3	18	3	18
4	25728	698598	3	89	2	69	2	70
5	102912	2786502	3	353	3	348	3	346
6	411648	11130246	3	1446	3	1440	3	1441

However, the Cartesian mesh is not the most economical way for discretizing the domain. Since our fully implicit $\mathbf{uv}p(3)$-TR-Q2/P1 FEM approach is also suitable for unstructured meshes (see Figure 20) that can better handle the far-field artificial boundary conditions with mesh-size independent time steps (here: $\Delta t = 2$ ms), it provides an excellent and practical alternative to structured methods (cf.

[18]). Thus, even large-scale problems can be solved in reasonable time (see Figure 23 and Table VII) in combination with locally adapted, unstructured meshes.

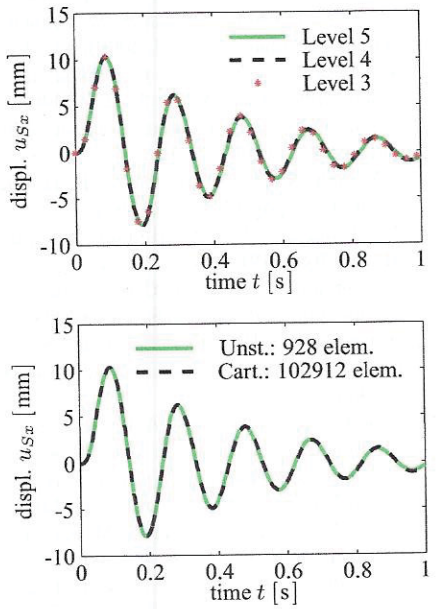

FIG. 23: Time history of horizontal displacement at point C using the **uvp**(3)-TR-Q2/P1 scheme for the unstructured grid (top) and both the Cartesian and unstructured grids (bottom) with optimal time step $\Delta t = 2$ ms. The corresponding number of elements and number of DOFs are given in Tables VI and VII.

TABLE VII: Averaged number of iterations and averaged CPU time in seconds (CPU) per time step for the multigrid solver in combination with **uvp**(3)-TR-Q2/P1 for $k^F = 10^{-2}$ m/s and $\Delta t = 2$ ms for the unstructured mesh. Level 3 is the mesh level of the multigrid coarse grid solver (here UMFPACK).

Mesh Level	#Elements	#Unknowns	#Iterations	CPU
3	928	25878	1	1.45
4	3712	101862	3	10.5
5	14884	404166	3	59
6	59392	1610118	3	243

7. CONCLUSION

In this paper, special numerical CFD techniques, which had been developed for the efficient simulation of incompressible flow problems, have been extended and applied to the set of DAEs governing a dynamic TPM model describing an intrinsically incompressible, elastic solid matrix that is saturated by an incompressible pore fluid. The model equations include the balance of momentum of the solid phase and the balance of momentum of the fluid phase as well as the mixture volume balance as algebraic side condition plus the solid velocity-displacement relation. This set of PDEs has been treated by a special variational form characterized by the absence of derivatives operating on the pressure functions and consideration of the fluid viscosity leading to a reduced and slightly different form of boundary conditions.

The spatial discretization within the mixed FEM has been carried out by the well-known (non-parametric) Q2/P1 finite element pair, which belongs to the best choices for incompressible flow problems in terms of efficiency, accuracy and robustness, while the discretization in time has been carried out by the standard θ-scheme ($\theta = 1/2$), which leads to a fully implicit, monolithic treatment of all variables involved. For the solution of the resulting (linear) systems of equations in each time step, a fast geometrical multigrid solver with special block Vanka smoother has been realized, which leads to convergence rates being independent of time step and mesh size, which is important particularly for large-scale problems. For validation purposes, canonical 1D and 2D wave propagation examples were opted from the related literature in order to validate and compare the presented approach with classical ones.

In conclusion, based on the comprehensive investigation of several test cases and the quantitative comparison with the results presented in [2], we recommend our fully implicit, monolithic approach using the uvp(3)-TR-Q2/P1 formulation in combination with the described special multigrid components. The proposed scheme does not only demonstrate excellent numerical results regarding accuracy and robustness, but is also less prone to stability issues (L-stability) of the time integrator even for coarser meshes.

In future works, we will investigate the potentially stabilizing influence of the fluid viscosity and account for the nonlinear convective terms. Moreover, an extension of our implementation to 3D and geometrically nonlinear and inelastic solid deformations is on the road map, which opens the avenue to more practically relevant applications.

Acknowledgments

We thank Michael Köster for the intensive support in the stage of implementing the presented model into FEATFLOW. Moreover, this work was partially supported by the German Research Foundation (DFG) under grant TU102/34-1.

[1] B. Markert, *Weak or Strong – On Coupled Problems in Continuum Mechanics* (Habilitation, Report No. II-20 of the Institute of Applied Mechanics (CE), University of Stuttgart, 2010).

[2] B. Markert, Y. Heider, and W. Ehlers, Int. J. Numer. Meth. Eng. **82**, 1341 (2010).

[3] R. de Boer, *Theory of Porous Media* (Springer-Verlag, Berlin, 2000).

[4] W. Ehlers, in W. Ehlers and J. Bluhm, eds., *Porous Media: Theory, Experiments and Numerical Applications* (Springer-Verlag, Berlin, 2002), pp. 3–86.

[5] B. Markert, in B. Markert, ed., *Extended and Multifield Theories for Continua* (Springer, 2011), vol. 59 of *Lecture Notes in Applied and Computational Mechanics*, pp. 129—-152.

[6] M. A. Biot, J. Appl. Phys. **12**, 155 (1941).

[7] M. A. Biot, J. Acoust. Soc. Am. **28**, 168 (1956).

[8] O. C. Zienkiewicz, A. H. C. Chan, M. Pastor, D. K. Paul, and T. Shiomi, Proc. R. Soc. Lond. **429**, 285 (1990).

[9] O. C. Zienkiewicz, A. H. C. Chan, M. Pastor, B. A. Schrefler, and T. Shiomi, *Computational geomechanics with special reference to earthquake engineering* (Wiley, Chichester, 1999).

[10] S. Diebels and W. Ehlers, Int. J. Numer. Methods Eng. **39**, 81 (1996).

[11] R. W. Lewis and B. A. Schrefler, *The Finite Element Method in the Static and Dynamic Deformation and Consolidation of Porous Media* (Wiley, Chichester, 1998), 2nd ed.

[12] S. Breuer, Transp. Porous Media **34**, 285 (1999).

[13] O. Coussy, *Mechanics of Porous Continua* (Wiley, Chichester, 1995).

[14] M. Schanz, *Wave Propagation in Viscoelastic and Poroelastic Continua: A Boundary Element Approach* (Lecture Notes in Applied Mechanics, Springer-Verlag Berlin Heidelberg, 2001).

[15] M. Schanz and S. Diebels, Acta Mech. **161**, 213 (2003).

[16] M. Schanz, Appl. Mech. Rev. **62**, 030803 (2009).

[17] H. Steeb, M. Frehner, and S. Schmalholz, in G. A. Maugin and A. V. Metrikine, eds., *Generalized Continua: One Hundred Years after the Cosserats* (Springer, 2010), pp. 179–190.

[18] Y. Heider, B. Markert, and W. Ehlers, Computational Mechanics **49**, 319 (2012).

[19] F. Brezzi and M. Fortin, *Mixed and Hybrid Finite Element Methods* (Springer-Verlag, New York, 1991).

[20] R. S. Sandhu and E. L. Wilson, J. Engng Mech. Div. ASCE **95**, 641 (1969).

[21] A. Prohl, *Projection and Quasi-Compressibility Methods for Solving the Incompressible Navier-Stokes Equations* (Teubner, Stuttgart, 1997).

[22] R. Rannacher, in P. Galdi, J. Heywood, and R. Rannacher, eds., *Fundamental Directions in Mathematical Fluid Mechanics* (Birkhäuser, Basel, 2000), pp. 191–293.

[23] M. Pastor, T. Li, X. Liu, O. C. Zienkiewicz, and M. Quecedo, Mech. Cohes. Frict. Mater. **5**, 511 (2000).

[24] X. Li, X. Han, and M. Pastor, Comput. Methods Appl. Mech. Engrg. **85**, 67 (2003).

[25] J. K. Suh, R. L. Spilker, and M. H. Holmes, Int. J. Numer. Methods. Engng **32**, 1411 (1991).

[26] A. Masud and T. J. R. Hughes, Comput. Methods Appl. Mech. Engrg. **191**, 4341– (2002).

[27] H. Damanik, J. Hron, A. Ouazzi, and S. Turek, Journal of Computational Physics **228**, 3869 (2009).

[28] H. Damanik, J. Hron, A. Ouazzi, and S. Turek, International Journal for Numerical Methods in Fluids **Volume 71, Issue 2**, 208 (2012).

[29] R. de Boer and W. Ehlers, Acta Mech. **83**, 77 (1990).

[30] B. Markert, Transp. Porous Med. **70**, 427 (2007).

[31] J. Heywood, R. Rannacher, and S. Turek, International Journal for Numerical Methods in Fluids **22**(5), 325 (Jan. 1996).

[32] S. Turek, J. Hron, M. Madlik, M. Razzaq, H. Wobker, and J. Acker, in H. Bungartz, M. Mehl, and M. Schäfer, eds., *Fluid-Structure Interaction II: Modelling, Simulation, Optimisation* (Springer, 2010), doi 10.1007/978-3-642-14206-2.

[33] R. de Boer, W. Ehlers, and Z. Liu, Arch. Appl. Mech. **63**, 59 (1993).

[34] Y. Saad and M. Schultz, SIAM J. Sci. Statist. Comput. **7**, 856 (1986).

[35] H. Van der Vorst, SIAM J. Sci. Stat. Comput. **13**, 631 (1992).

[36] G. Strang, *Computational Science and Engineering* (Wellesley-Cambridge press, London, 2007).

[37] S. Turek, *Efficient solvers for incompressible flow problems: An algorithmic and computational approach* (Springer, 1999).

[38] H. Wobker and S. Turek, Advances in Applied Mathematics and Mechanics **1**(1), 29 (2009).

[39] S. P. Vanka, Journal of Computational Physics **65**, 138 (1986).

[40] O. von Estorff, Computers & Structures **38**, 289 (1991).

[41] O. von Estorff and M. Firuziaan, Eng. Anal. Boundary Elem. **24**, 715 (2000).

[42] D. Kim and C. Yun, Int. J. Numer. Methods Eng. **47**, 1241 (2000).

[43] http://www.featflow.de